

Autoinhibition and relief mechanisms for MICAL monooxygenases in F-actin disassembly

Received: 16 February 2024

Accepted: 25 July 2024

Published online: 09 August 2024

 Check for updatesLeishu Lin^{1,2,6}, Jiayuan Dong^{1,2,6}, Shun Xu^{1,2}, Jinman Xiao^{3,4}, Cong Yu^{3,4,5}, Fengfeng Niu^{1,2}✉ & Zhiyi Wei^{1,2,5}✉

MICAL proteins represent a unique family of actin regulators crucial for synapse development, membrane trafficking, and cytokinesis. Unlike classical actin regulators, MICALs catalyze the oxidation of specific residues within actin filaments to induce robust filament disassembly. The potent activity of MICALs requires tight control to prevent extensive damage to actin cytoskeleton. However, the molecular mechanism governing MICALs' activity regulation remains elusive. Here, we report the cryo-EM structure of MICAL1 in the autoinhibited state, unveiling a head-to-tail interaction that allosterically blocks enzymatic activity. The structure also reveals the assembly of C-terminal domains via a tripartite interdomain interaction, stabilizing the inhibitory conformation of the RBD. Our structural, biochemical, and cellular analyses elucidate a multi-step mechanism to relieve MICAL1 autoinhibition in response to the dual-binding of two Rab effectors, revealing its intricate activity regulation mechanisms. Furthermore, our mutagenesis study of MICAL3 suggests the conserved autoinhibition and relief mechanisms among MICALs.

Actin, as one of the major components of the cytoskeleton, plays a fundamental role in maintaining and regulating cell morphology and numerous functions, including cell migration, contraction, division, endocytosis, and intracellular trafficking. These functions rely on the intrinsic property of actin to dynamically transition between its monomeric, globular (G-actin) and polymeric, filamentous (F-actin) forms, as well as higher-ordered bundles and networks^{1–5}. To regulate actin dynamics, a variety of actin regulator proteins have been identified over the past few decades, such as the Arp2/3 complex, formins, ADF/cofilin, and gelsolin. These regulators modulate the transition between G-actin and F-actin through physical and non-covalent interactions^{5–8}.

MICAL (Molecule Interacting with CasL) proteins have recently emerged as novel F-actin disassembly factors^{9,10}, playing roles in various cellular functions. In *Drosophila*, MICAL is critical for repulsive axon guidance and bristle development by directing actin cytoskeleton reorganization^{10–13}. In mammals, three MICAL isoforms were identified¹⁰. MICAL1 is required for synapse development^{14,15}, while both MICAL1 and MICAL3 contribute to cytokinesis and vesicle trafficking by regulating F-actin disassembly^{16–19}. Additionally, MICAL2 has been implicated in cancer cell functions and is considered a potential drug target^{20,21}.

Unlike classical actin regulators, MICAL proteins possess monooxygenase (MO) enzymatic activity to covalently oxidize specific

¹Shenzhen Key Laboratory of Biomolecular Assembling and Regulation, Shenzhen, Guangdong, China. ²Department of Neuroscience and Brain Research Center, School of Life Sciences, Southern University of Science and Technology, Shenzhen, Guangdong, China. ³Department of Chemical Biology, School of Life Sciences, Southern University of Science and Technology, Shenzhen, Guangdong, China. ⁴Guangdong Provincial Key Laboratory of Cell Micro-environment and Disease Research, and Shenzhen Key Laboratory of Cell Microenvironment, Shenzhen, Guangdong, China. ⁵Institute for Biological Electron Microscopy, Southern University of Science and Technology, Shenzhen, Guangdong, China. ⁶These authors contributed equally: Leishu Lin, Jiayuan Dong. ✉e-mail: niuff@sustech.edu.cn; weizy@sustech.edu.cn

methionine residues of actin, resulting in robust actin filament disassembly^{12,22,23}. Notably, actin oxidized by MICALs is not directly replenished into the G-actin pool in cells, which requires additional chemical modification by MsrB reductase^{24,25}. Thus, the profound impact of the MICAL-mediated modification requires tight control mechanisms to prevent extensive disruption to cellular actin organization. Malfunction of MICALs is associated with several human diseases, including cancers and neurological disorders, due at least in part to uncontrolled MICAL activity^{26–29}.

MICAL proteins consist of four folded domains, from the N-terminal catalytic MO domain to the C-terminal Calponin Homology (CH) domain, Lin-11/Is1-1/Mec-3 (LIM) domain, and Rab-binding domain (RBD), connected by three loops (L1, L2, and L3) (Fig. 1a)³⁰. While the MO domain catalyzes the oxidation modification of actin filaments with the assistance of its cofactors, FAD and NADPH^{22,31,32}, the C-terminal domains are proposed to regulate MO activity through forming an autoinhibited/closed state^{15,18,33}. Effector proteins, such as Rab8a-subfamily GTPases and Plexins, can locally activate MICALs by binding to the RBD^{10,18,34}. Despite extensive studies on individual domain structures^{19,31,34–41}, the molecular mechanisms underlying the autoinhibition formation and relief of MICALs remain poorly understood due to the lack of structural information on full-length MICAL proteins.

Here, we reported the cryo-EM structure of full-length MICAL1, revealing its hammer-like autoinhibited/closed conformation. In this structure, the RBD binds to the MO domain and allosterically inhibits its enzymatic activity. Interestingly, a tripartite assembly of the CH, LIM, and RBD domains is required for the inhibitory binding of the RBD. Through a combination of structural, biochemical, and cellular analyses, we demonstrated that the simultaneous binding of two Rab molecules to the RBD induces a series of conformational changes in the RBD, leading to the disruption of the autoinhibited conformation. In addition, our results indicated a conservation of the autoinhibition

mechanism among MICAL family proteins. Taken together, our findings uncover the autoinhibition and relief mechanisms of MICAL proteins, advancing our understanding of these unique actin regulators in regulating actin dynamics to achieve its diverse cellular functions.

Results

Overall structure of full-length MICAL1 in the autoinhibited state

To elucidate the regulatory mechanism of MICAL family proteins in controlling F-actin depolymerization, we purified the full-length protein of human MICAL1 (Fig. 1b). Consistent with the previous report³⁴, the purified MICAL1 protein predominantly exists as a monomer in solution (Fig. 1b) and shows a minimal enzymatic activity compared to the fully activated MO domain alone (Fig. 1c), indicating that the full-length MICAL1 adopts a monomeric, autoinhibited, and closed conformation. Despite extensive trials, efforts to crystallize the autoinhibited MICAL1 structure using the purified protein were unsuccessful. Therefore, we turned to determine the structure using the cryo-EM technique. Initial analysis of the MICAL1 sample using negative-staining EM revealed a significant portion of particles with a compact shape (Supplementary Fig. 1a). However, in cryo-EM analysis, while some particles adopted a similar compact shape, indicating the interdomain interaction between the N-terminal MO domain and the C-terminal CH-LIM-RBD (CLR) region (class-I in Fig. 1d, and Supplementary Fig. 1b, c), the majority of particles had only the MO domain to be well-aligned (class-II in Fig. 1d, and Supplementary Fig. 1b, c), likely due to a disruption of the interdomain interaction of MICAL1 induced by freezing damage during cryo-sample preparation. To stabilize the interdomain interaction, glutaraldehyde (GA) was used for cross-linking. The GA-treated sample exhibited a significant improvement in maintaining the compact shape during sample freezing (Supplementary Fig. 1c), which was therefore used for the following cryo-EM structure determination. With a combination of multiple methods for

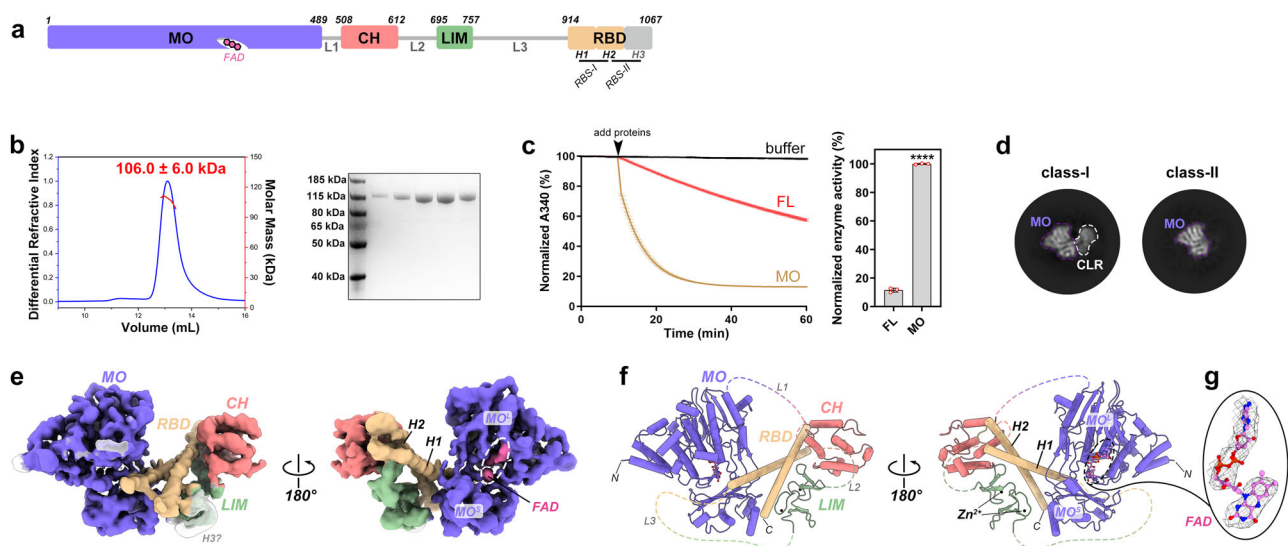


Fig. 1 | Biochemical and cryo-EM characterization of human MICAL1. **a** Domain organization of human MICAL1. The four domains, monoxygenase (MO), CH, LIM, and Rab-binding domain (RBD), are interconnected by three loops (L1-L3). Two Rab-binding sites (RBS-I/II) in the RBD are indicated. The cofactor FAD bound in the MO domain is highlighted, which is essential for enzymatic activity. **b** Analytical size-exclusion chromatographic (aSEC) and SDS-PAGE analyses of the purified MICAL1 sample. The aSEC analysis was coupled with multi-angle static light scattering for molecular weight determination. **c** Enzymatic activity measurements of the MO fragment and full-length MICAL1. The enzymatic activities were measured using a NADPH-consumption assay. Protein concentration of 1 μ M was used. The results were normalized against the activity of the MO fragment.

Three independent repeats were performed for each condition. **d** Representation of two 2D classes of MICAL1 particles, showing the two conformations of MICAL1 observed in cryo-EM analysis. **e**, **f** The cryo-EM map (**e**) and corresponding atomic model (**f**) of full-length MICAL1 in the autoinhibited state. Each domain is colored using the same code as that in panel (**a**). The large and small lobes (MO^L and MO^S) in the MO domain and the two helices (H1 and H2) in RBD are labeled. An unassigned piece of density is highlighted transparently in panel (**e**). The L1-L3 loops missing in the density map are indicated by dash lines, and the N/C-termini of the atomic model of full-length MICAL1 are labeled (**f**). **g** Density-fit-model showing the presence of the cofactor FAD in the MO domain. The map counter level is set to 0.1.

particle picking and particle orientation optimization, we successfully reconstituted a density map of full-length MICAL1 with an overall resolution of 3.94 Å (Fig. 1e, Supplementary Fig. 2, and Supplementary Table 1). This high-resolution map allowed us to build an atomic model for most regions of MICAL1, except for the domain-connecting loops and the last helix in the RBD (Fig. 1f and Supplementary Movie 1).

The autoinhibited structure of MICAL1 adopts a hammer-like shape, with the N-terminal MO domain and the C-terminal CLR region forming the ‘hammerhead’ and ‘handle’, respectively (Fig. 1e, f). In this autoinhibited structure, the MO domain resembles previously reported crystal structures of the MO fragment^{35–37,39}, comprising a large lobe (MO^L) and a small lobe (MO^S), with the active site harboring a FAD molecule within a cleft formed by these lobes (Fig. 1e–g, and Supplementary Fig. 3a). In the CLR region, the CH and LIM domains, while sharing structural similarities with their respective fragment structures, have their poses distinct from those previously proposed (Supplementary Fig. 3b–d)^{34,37,39}, through assembling with the RBD to form the compact ‘handle’ structure. Specifically, the CH domain interacts with the RBD to create a groove that encapsulates the LIM domain (Fig. 1f). The assembled CLR region packs with the MO domain via the direct binding of the RBD to another cleft in the MO domain, positioned opposite to the FAD-binding cleft (Fig. 1f). This head-to-tail interaction aligns with the proposed inhibitory effect of the RBD on the MO activity of MICAL proteins^{15,18,33}. Notably, unlike the three-helix structure observed in the RBD fragment (Supplementary Fig. 3e)³⁸, only the first two helices (H1 and H2) can be confidently assigned in the autoinhibited structure (Fig. 1f), while the density of the third helix (H3) is largely smear (Fig. 1e), suggesting high conformational dynamics of H3 in the RBD.

MO activity is inhibited via the MO/RBD interaction

In the hammer-like MICAL1 structure, the MO/RBD interaction connects the head and tail of MICAL1 for the autoinhibition formation. In addition to the FAD-binding cleft, the MO domain contains a shallower cleft on the opposite side (Fig. 1f and Supplementary Fig. 3a), accommodating the H1 helix of the RBD (Fig. 2a). The H1-binding cleft is mainly formed by the loops connecting β 17 and α 15, β 9 and β 10, β 14 and β 15 in the MO^L lobe (Fig. 2b), and β 11 and its flanking sequence in the MO^S lobe (Fig. 2c). The RBD employs F925 in H1 to interact with a small hydrophobic patch formed by P401, L402, and V285 in the MO domain (Fig. 2b). Conversely, two hydrophobic residues I264 and Y265 in the MO^S lobe are embedded into a hydrophobic crevice formed by the H1 and H2 helices (Fig. 2c). In addition to the hydrophobic interactions, the MO/RBD interaction is further enhanced by hydrogen bonding (Fig. 2b, c). Notably, R933 in H1 forms a cation- π interaction with F399 in the β 17/ α 15 loop, stabilizing the sidechain orientation of R933 and thereby allowing it to form two hydrogen bonds with the mainchain atoms of the β 14/ β 15 loop (Fig. 2b).

Despite the interaction between the RBD and the MO domain in the autoinhibited MICAL1 structure, the active site of the MO domain seems to remain accessible for catalysis (Fig. 1f and Supplementary Fig. 3a). This raises the question of how MO activity is suppressed through RBD binding. Previous structural studies of the MO domain of MICAL1 have shown that the isoalloxazine ring in the FAD head flips after NADPH treatment during catalysis, resulting in conformational changes in several residues at the active site³⁶. As the RBD-binding cleft and the active site are separated only by the loop between β 17 and α 15 (Fig. 2d and Supplementary Fig. 3a), RBD binding may interfere with the active site dynamics, inhibiting FAD-mediated catalysis. To verify this hypothesis, we compared the MO domain in the autoinhibited conformation with the crystal structures of the MO fragment in the reduced (MO^{red}, with NADPH treatment) and oxidized (MO^{ox}, without NADPH treatment) states, respectively (Fig. 2e, f). While the autoinhibited MO and MO^{ox} are highly similar in their active site conformations (Fig. 2e), the MO^{red} shows significant differences in the

loops surrounding the bound FAD molecule, accompanied by the conformational changes in F399, W400, and P401 in the loop between β 17/ α 15 and H126 in the β 3 flanking loop (Fig. 2f). Notably, the aromatic sidechain of F399^{MO} undergoes a large rotation upon NADPH treatment (Fig. 2f), disrupting the cation- π interaction with R933^{RBD} observed in the autoinhibition state (Fig. 2b). These changes impose steric hindrance for the binding of the RBD to the MO^{red}. Conversely, the MO/RBD interaction stabilizes the MO^{ox} conformation at the active site, preventing the conformational transition of the bound FAD from the oxidized state to the reduced state (Fig. 2g). Given the essential role of FAD in redox catalysis, the MO/RBD interaction effectively blocks enzymatic activity in autoinhibited MICAL1. On the other hand, as previously proposed, this RBD-binding shallower cleft in MO might include a tunnel for substrate access to the active site³⁶, the direct interaction of RBD to the MO observed in the autoinhibited MICAL1 would coincidentally block this tunnel, further inhibiting MO activity by preventing the enzyme and substrate contact.

To validate our structural findings, we designed three mutations targeting key interface residues, including F925A and R933A in the MO^L/RBD interface and I264Q in the MO^S/RBD interface, aiming at disrupting the MO/RBD interaction. Indeed, as indicated by the NADPH-consumption assay, these interface mutants showed significantly increased enzymatic activity, compared to wild-type MICAL1 (Fig. 2h), confirming the inhibitory role of the RBD in modulating MO activity. In addition to the *in vitro* assay, we further analyzed the disruptive effects of the MO/RBD interaction on cellular actin filaments, considering MICAL1’s monooxygenase activity in disassembling actin filaments in cells³³. By transfecting MICAL1 and its interface mutants into HeLa cells, we found that, in contrast to cells overexpressing wild-type MICAL1 with a normal distribution of actin filaments (Figs. 2i, 4d), overexpression of the interface mutants led to an obvious reduction in actin filaments (Figs. 2i, 4d), further supporting the inhibitory effect of the RBD on MO activity via the direct MO/RBD interaction.

The compact structure of CH-LIM-RBD is required for autoinhibition formation

Although the RBD binding directly blocks MO activity in autoinhibited MICAL1, the purified RBD fragment alone did not show either detectable binding to the MO domain or inhibit MO activity, as indicated by aSEC analysis (Fig. 3a) and NADPH-consumption assay (Fig. 3b, c). Interestingly, the purified CLR fragment could interact with the MO domain and reduce its activity (Fig. 3b–d). To further confirm CLR inhibits MO activity through the MO/RBD interaction, we measured the MO activity by adding the mutated CLR^{F925A} fragment. As indicated by NADPH-consumption results, the F925A mutation indeed hindered the suppressive effect of CLR on the MO activity (Fig. 3b, c). Our biochemical findings suggest that the CH and LIM domains are required for suppressing MO activity, despite lacking direct contact with the MO domain in the autoinhibited MICAL1 structure (Fig. 3f). The CH and LIM domains form the compact ‘handle’ structure with the RBD through the tripartite CH/LIM/RBD interaction (Fig. 3f), in which the CH domain binds to the N-terminal region of the H2 helix, creating a hydrophobic groove in conjugation with H1 (Fig. 3g). This groove grasps a protruded loop from the first zinc-finger motif of the LIM domain through extensive hydrophobic interactions among Y705, V706, and L707 at this loop tip of the LIM domain, L589 and A602 in the CH domain, and L945, V950, L952, L956, L974, and V978 in the RBD (Fig. 3g). Disrupting the tripartite interaction by designed interface mutations, especially the V706Q/L707Q mutation that presumably blocks the hydrophobic core formation at the tripartite interface, led to an increased NADPH consumption rate in solution (Fig. 3h) and diminished actin filaments in cells (Figs. 3i, 4d). These results indicate that the suppression of MO activity requires the assembly of the entire CLR region.

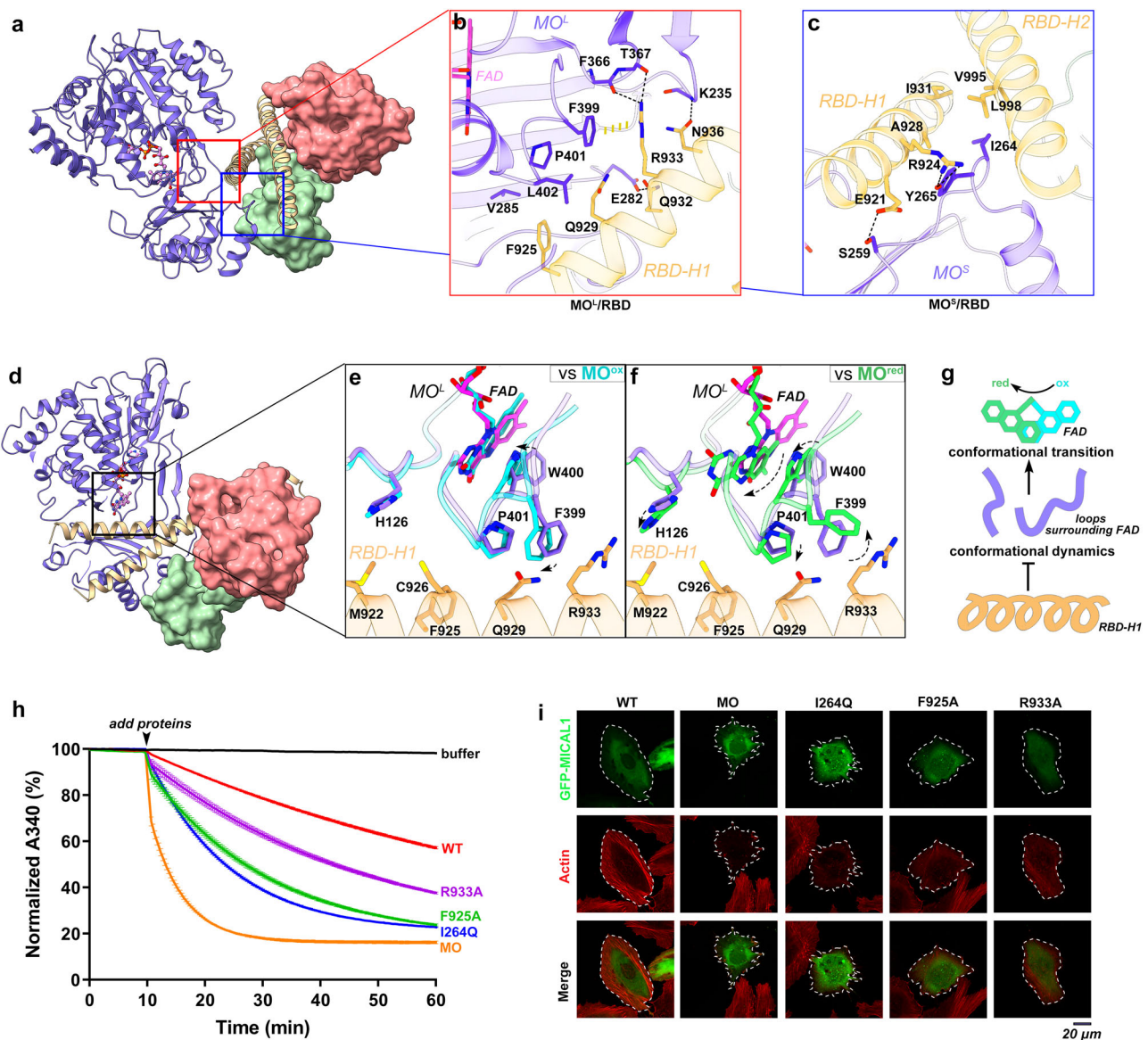


Fig. 2 | MO/RBD interaction facilitates the activity inhibition of MICAL1.

a–c The MO/RBD interaction observed in the autoinhibited MICAL1 structure (**a**), highlighting the critical interactions at the MO^L/RBD (**b**) and MO^S/RBD (**c**) interfaces. **d–f** Structural comparisons showing conformational differences in the MO domain of autoinhibited MICAL1 (**d**) compared to the MO fragments in oxidated (MO^{ox}, PDB: 2BRY) (**e**) or reduced (MO^{red}, PDB: 2C4C) (**f**) conditions. The binding of the RBD to the MO limits the conformational changes of FAD and the surrounding

loops. **g** Schematic diagram illustrating the inhibitory mechanism of the MO domain by the RBD. **h** NADPH-consumption measurements of MICAL1 and the MO/RBD interface mutants. Protein concentration of 1 μM was used. Three independent repeats were performed for each condition. **i** Confocal imaging of HeLa cells overexpressing GFP-tagged MICAL1 and the MO/RBD interface mutants. Actin filaments were stained by fluorescence-labeled phalloidin. Cell edges were indicated by dashed lines for reference.

To further confirm the critical role of the compact CLR fold in blocking MO activity, we analyzed the CLR-mediated inhibitory effect using the V706Q/L707Q mutation. In line with the loosely packed CLR mutant structure caused by the disrupted tripartite CLR interaction, the elution peak of the CL^{V706Q/L707Q}R protein shifted forward in our aSEC analysis, compared to that of wild-type CLR (Fig. 3d). In contrast to wild-type CLR, CL^{V706Q/L707Q}R neither interacts with the MO fragment (Fig. 3e) nor shows a potent inhibition on MO activity (Fig. 3b, c). Additionally, CL^{V706Q/L707Q}R lost its capability to impede the binding of the MO domain to F-actin, as indicated by our F-actin co-sedimentation assay (Fig. 3j and Supplementary Fig. 4). Taken together, our structural, biochemical, and cellular results demonstrate that the tripartite interaction of the CLR region is essential in maintaining the autoinhibited conformation of MICAL1. It is likely that the dynamic structure of the RBD prevents it from adopting the MO-bound

conformation observed in the autoinhibited structure of MICAL1, whereas the tripartite interaction in the CLR region stabilizes the MO-bound conformation of the RBD, promoting the MO binding and suppressing MO activity in both substrate (F-actin) binding and NADPH-dependent catalysis.

Dual disruption of the MO/RBD and CH/LIM/RBD interactions effectively releases MICAL1's autoinhibition

The interface mutations disrupting either the MO/RBD or CH/LIM/RBD interaction partially enhance MICAL1's activity in NADPH turnover (Figs. 2h, 3c), however, at a much lower level (less than 40%) than the fully activated MO fragment (Fig. 4a, b, and Supplementary Fig. 5a), suggesting that disruption of either interdomain interaction alone may not be sufficient to fully unleash the activity of MICAL1. Thus, we selectively combined two single-interface mutations, generating

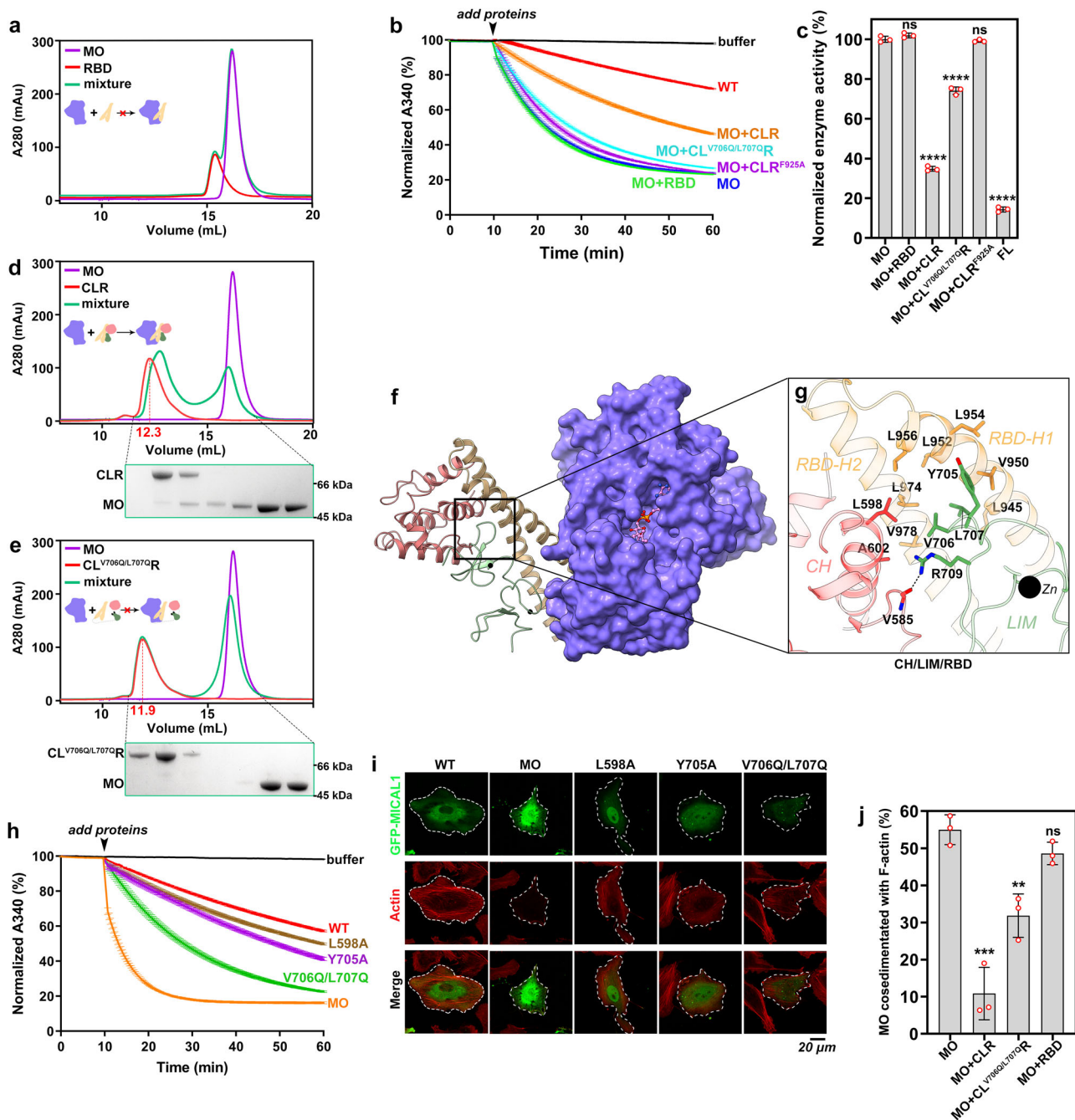


Fig. 3 | Suppression of MO activity and actin binding by the tripartite CH-LIM-RBD interaction. **a** aSEC profiles showing no detectable binding between the fragments of MO and RBD. **b, c** NADPH-consumption measurements (**b**) and statistical analysis (**c**) depicting the impact of the addition of the RBD, CLR, or CLR mutant (10 μ M) on the activity of the MO domain (0.5 μ M). The V706Q/L707Q mutation was designed to destabilize the compact CLR structure in the autoinhibited state. **f, g** The tripartite CH/LIM/RBD interface observed in the autoinhibited MICAL1 structure. **h, i** NADPH-consumption measurements (**h**) and confocal imaging of HeLa cells (**i**) of MICAL1 and the CH/LIM/RBD interface mutants. The protein concentration of 1 μ M was used in the NADPH-consumption assay. Three independent repeats were performed for each condition in the NADPH-consumption measurements. **j** Quantification analysis of F-actin co-sedimentation results with the MO fragment, with or without the addition of the indicated fragments. The co-sedimentation results are presented in Supplementary Fig. 4c. Three independent repeats were performed for each condition.

mutant (**e**). The backward shift of the CLR peak indicates a more compact CLR structure in the autoinhibited state. **f, g** The tripartite CH/LIM/RBD interface observed in the autoinhibited MICAL1 structure. **h, i** NADPH-consumption measurements (**h**) and confocal imaging of HeLa cells (**i**) of MICAL1 and the CH/LIM/RBD interface mutants. The protein concentration of 1 μ M was used in the NADPH-consumption assay. Three independent repeats were performed for each condition in the NADPH-consumption measurements. **j** Quantification analysis of F-actin co-sedimentation results with the MO fragment, with or without the addition of the indicated fragments. The co-sedimentation results are presented in Supplementary Fig. 4c. Three independent repeats were performed for each condition.

double-interface mutations to interfere with both interdomain interactions simultaneously. Compared to the single-interface mutations, the double-interface mutations, including L598A/F925A and Y705A/F925A, exhibit significantly higher enzymatic activity (Fig. 4a, b, and Supplementary Fig. 5a). Notably, the Y705A/F925A mutant of MICAL1 showed activity comparable to the MO fragment (Fig. 4a, b). Consistent

with the NADPH consumption results, the overexpression of the L598A/F925A and Y705A/F925A mutations showed a more pronounced impairment of actin filament distribution at a level comparable to the MO fragment in HeLa cells (Fig. 4c, d, and Supplementary Fig. 5b). Similarly, the cell size reduction observed in cells overexpressing these two double-interface mutations is more severe than that with the

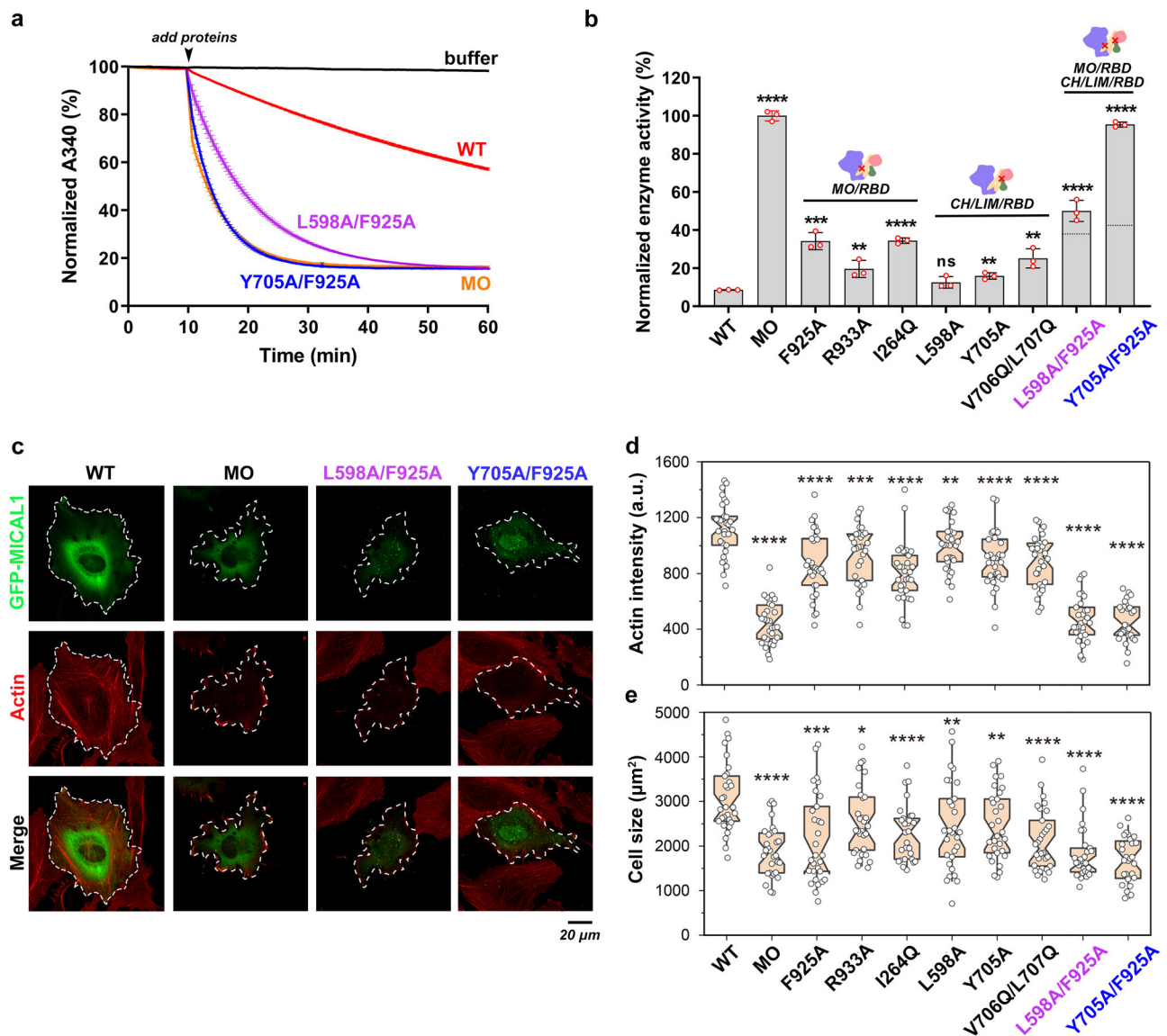


Fig. 4 | Disruption of both interfaces effectively releases MICAL1 autoinhibition. **a** NADPH-consumption measurement of MICAL1 and its double-interface mutants. Protein concentration of 1 µM was used. Three independent repeats were performed for each condition. **b** Statistical analysis of the single-interface and double-interface mutants of MICAL1. The results were normalized against the activity of the MO fragment. The corresponding NADPH-consumption curves are presented in Figs. 2h, 3h, and panel (a). The dot lines in the activity bars of the L598A/F925A and Y705A/F925A mutants indicate the expected additive effects of the two corresponding single-interface mutants over the basal activity of WT. The calculated additive impact is lower than the actual activity of the double-interface

mutants, suggesting that the double-interface mutants contribute a cooperative effect to the disruption of autoinhibition formation. Three independent repeats were performed for each condition. **c** Confocal imaging of HeLa cells expressing GFP-tagged MICAL1, MO, and the double-interface mutants. **d**, **e** Statistical analyses of cellular actin intensity (**d**) and cell size (**e**) in HeLa cells overexpressing GFP-tagged MICAL1 and its variants. Data from 30 cells were analyzed for each condition. An exception was noted for the Y705A/F925A mutant, where data from 28 cells were analyzed. Representative cell imaging data for all conditions are shown in Figs. 2i, 3i, and panel (c).

single-interface mutations, resembling the effect seen with the MO fragment (Fig. 4e). Altogether, our biochemical and cellular results not only demonstrate the importance of both interdomain interactions in MICAL1 autoinhibition but also suggest the requirement of simultaneously disrupting these interactions for MICAL1 activation.

Interestingly, although the interdomain loops are not conserved and are invisible in the cryo-EM structure (Supplementary Fig. 6a), the L1 loop has a relatively fixed length of ~20 residues among MICAL proteins in vertebrates (Supplementary Fig. 6b). Considering that the distance between the MO C-terminus and CH N-terminus is ~54 Å (Supplementary Fig. 6a), aligning closely with the length of a fully stretched loop with 19 residues⁴², the L1 loop is likely to adopt a highly stretched conformation. This structural observation suggests the role

of L1 in maintaining the spatial arrangement between the ‘hammer-head’ and ‘handle’ structures in autoinhibited MICAL1. Consistently, shortening the L1 loop by deleting 10 residues (residues 494–503) resulted in a substantial relief of MICAL1 autoinhibition (Supplementary Fig. 6c, d). In contrast, deletions within the L3 loop (Δ TBM^{800–822} and Δ PRM^{823–843}), specifically targeting the binding sequences for myosin Va¹⁹ and ASAP1⁴⁰, had minimal impact on the relief of MICAL1 autoinhibition (Supplementary Fig. 6c, d). While the specific roles of L2 and L3 are not evident from the current data, given the structural role in connecting the domains in the CLR region and the importance of CLR in controlling MICAL activity, we speculate that the L2 and L3 loops may have regulatory functions in the autoinhibition and activation of MICAL family proteins.

A conformational transition of the H3 helix regulates MICAL1's activity upon Rab binding

In cells, MICALs are recruited to specific cellular locations and relieved from their autoinhibition state via the binding of their RBDs to effectors, such as Rab8-subfamily GTPases (e.g., Rab8 and Rab10) and neuroreceptor Plexins, thereby allowing efficient activation to modify the local distribution of actin filaments^{10,15,18,38}. However, the relief mechanism of MICALs' autoinhibition mediated by these effectors remains unclear. Given the crucial role of the RBD in regulating MICAL1's autoinhibition (Fig. 1a)³⁸, we compared crystal structures of the RBD fragment in the apo and Rab-bound forms with the autoinhibited MICAL1 structure, respectively. As indicated in Fig. 5a–c, the C-terminal position of the H3 helix in either the apo or Rab-bound RBD would lead to atomic clashes with the CH domain in the autoinhibited state. This analysis suggests that the autoinhibited state cannot accommodate the three-helix structure of the RBD. Thus, the H3 helix may unfold from the three-helix structure of the RBD upon autoinhibition formation, providing a plausible explanation for the invisible H3 helix in the autoinhibited structure. Conversely, the foldback of the H3 helix might trigger the transition from autoinhibition to an open conformation (Fig. 5a–c and Supplementary Fig. 7a). Thus, the conformational dynamics allow H3 to function as a switch for regulating MICAL1's activity.

To validate the role of H3 in controlling MICAL1's activity, we truncated the H3 helix to create a shortened variant of MICAL1 (MICAL1¹⁻¹⁰⁵⁵) by deleting the C-terminal 12 residues. Since the H3 C-terminus may clash with the CH domain upon Rab binding (Fig. 5c), this shortened variant likely diminishes the activation effect of Rab binding. As expected, while full-length MICAL1 showed a ~4-fold enhancement in NADPH turnover upon adding Rab8a, the MICAL1¹⁻¹⁰⁵⁵ only displayed a 2-fold activation effect of Rab8a (Fig. 5g, h). Next, we analyzed the impact of Rab binding on MICAL1 activation in the presence of the physiological substrate F-actin. Consistent with the NADPH consumption results, MICAL1 and MICAL1¹⁻¹⁰⁵⁵ exhibited weak activity in F-actin depolymerization, whereas the MO fragment and the Y705A/F925A mutant that has been demonstrated to abolish MICAL1 autoinhibition formation showed much stronger capabilities in depolymerizing F-actin (Fig. 5i). However, upon Rab8a addition, unlike the accelerated F-actin disassembly rate of wild-type MICAL1, the rate enhancement was significantly reduced for MICAL1¹⁻¹⁰⁵⁵ (Fig. 5i). Additionally, it is noteworthy that a disease-associated frame-shifting mutant A1065fs, which lengthens the H3 helix with an excess of 59 amino acids, boosted MICAL1's activity in cells^{27,43}, further confirming the crucial role of H3 in regulating the autoinhibition formation and relief of MICAL1.

Dual Rab-binding potentially drives effective relief of MICAL1 autoinhibition according to structural analysis

The RBD contains two Rab-binding sites, RBS-I and RBS-II³⁸. As RBS-II is comprised of the H2 and H3 helices, once a Rab molecule (e.g., Rab10) binds onto RBS-II in autoinhibited MICAL1, the potential foldback of H3 is likely to push the CH domain away due to the steric clash (Fig. 5c), thereby disrupting the CLR assembly. Following the dissociation of the CH domain from the tripartite interface, RBS-I, formed by the H1 and H2 helices, which is initially concealed by the CH domain in the autoinhibited state, becomes accessible for another Rab binding (Fig. 5c). The binding of the second Rab molecule (Rab10') to RBS-I induces a change in the H1 orientation, resulting in a rotation of the N-terminal part of H1 (Fig. 5d). Such a rotational change of H1 not only moves F925 away from the hydrophobic patch in the MO cleft (Fig. 5e) but also disrupts the cation- π interaction between R933 and F399 (Fig. 5f). Consequently, the MO/RBD interaction is destabilized by the second Rab molecule, therefore releasing the RBD-mediated suppression of MO activity.

To investigate the roles of RBS-I and RBS-II in response to Rab binding, we introduced two distinct mutations: V978A in H2 and V1041Q in H3 (Supplementary Fig. 7a)³⁸, which abolish the binding of Rab8a to RBS-II and RBS-I, respectively (Supplementary Fig. 7b). Consistent with our structural analysis, the NADPH-consumption assay showed that both the single-site mutations and the double-site mutation weakened the capability of Rab8a for releasing MICAL1 activity (Fig. 5g, h), indicating both RBS-I and RBS-II are required for the Rab-mediated relief of MICAL1 autoinhibition. Likewise, as shown in Fig. 5i, the V978A or V1041Q mutant failed to show Rab8a-promoted activity in depolymerizing F-actin. Altogether, our results suggest that the simultaneous binding of Rab8-subfamily proteins at the two RBSs of the RBD effectively drives the relief of MICAL1 autoinhibition, releasing MO activity for F-actin disassembly.

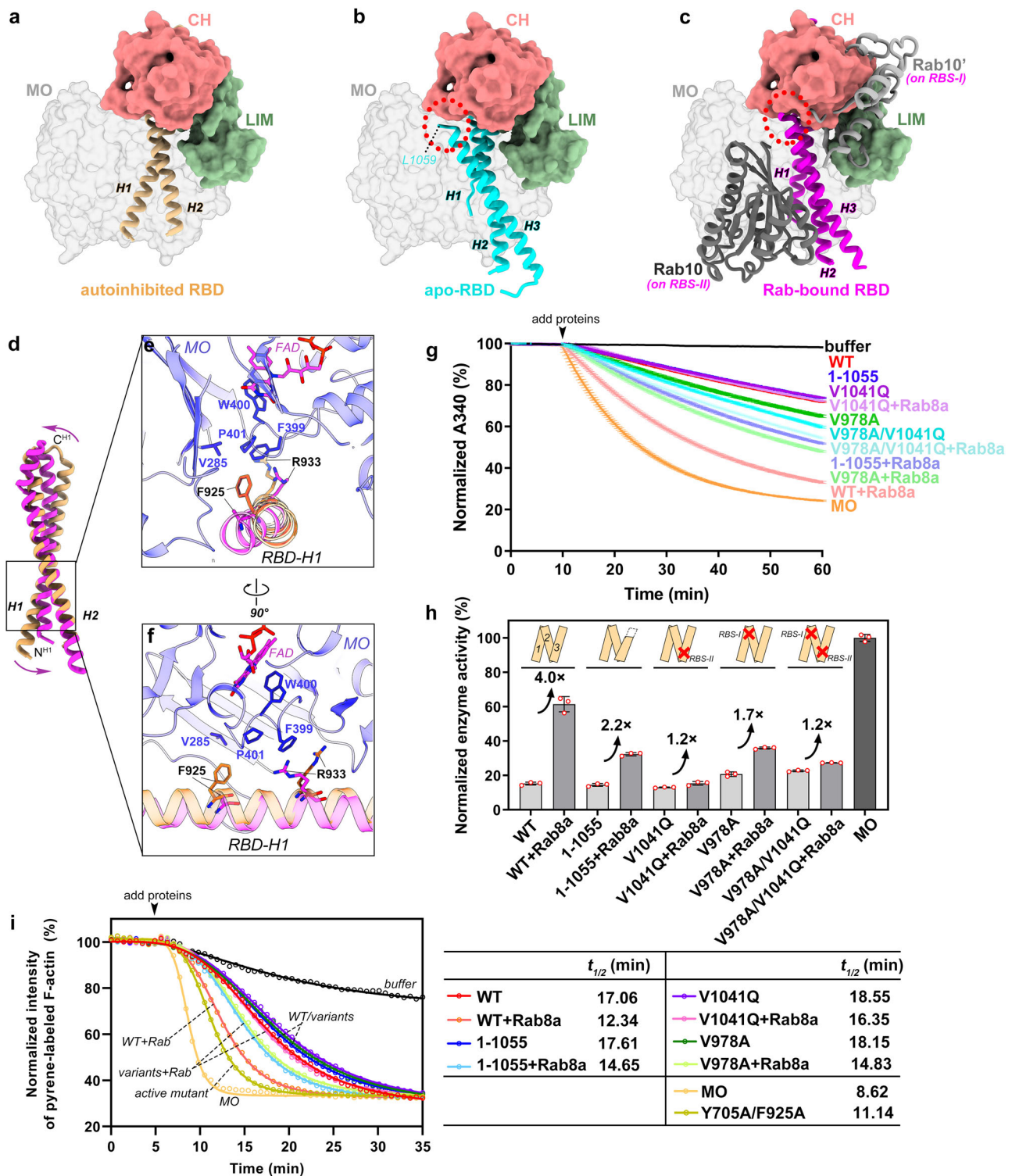
MICAL3 employs similar mechanisms for autoinhibition formation and relief

Our amino acid sequence analyses showed that the interface residues observed in the autoinhibited MICAL1 structure are highly conserved across members of the MICAL family from human to fly (Supplementary Fig. 8a–e), indicating a shared autoinhibition mechanism among MICAL proteins. To validate this, we applied interface mutations in MICAL3 (Fig. 6a) that correspond to those shown to have disruptive effects on MICAL1 autoinhibition (Fig. 4b, e). Among these mutations in MICAL3, L610Q (corresponding to the L598A mutation in MICAL1) was designed to generate a stronger disruption of the hydrophobic CH/RBD interface. As expected, overexpression of all six mutants of MICAL3 significantly reduced both the cellular level of actin filaments and the cell size (Fig. 6b–d), confirming the conservation of autoinhibition formation among MICALs. Interestingly, unlike the mild disruptive effect of the single interface mutations of MICAL1, the L1839A and V773Q mutations in MICAL3 (equivalent to the F925A and V706Q mutations in MICAL1, respectively) showed a strong disruption in actin filaments (Fig. 6c), suggesting potential differences in the autoinhibition conformation between MICAL1 and MICAL3. Given the significantly extended loop lengths of L2 and L3 in MICAL3 as compared to MICAL1 (Supplementary Fig. 8a), these long loops in MICAL3 may regulate the assembly of the compact CLR structure through steric impacts, thereby influencing the autoinhibition conformation and contributing to the observed differences between MICAL1 and MICAL3. In addition, in line with the previous finding that MICAL3's RBD is capable of binding to two Rab molecules simultaneously³⁸, the residues at the two Rab-binding sites on the RBDs of MICALs are also highly conserved (Supplementary Fig. 8e). The conserved nature of the Rab binding sites suggests a similar mechanism for releasing MICAL3 autoinhibition through dual Rab binding. Together, MICAL proteins are likely to share similar mechanisms in autoinhibition formation and relief to tightly control their enzymatic activity for regulating actin filament dynamics in various cellular compartments.

Discussion

In this study, we determined the autoinhibited structure of MICAL1 and revealed the autoinhibition mechanism that involves the entire C-terminal CLR region. Based on our structural findings and biochemical and cellular analyses, we proposed a model for the Rab-mediated relief of MICAL autoinhibition with the following steps (Fig. 6e and Supplementary Movie 2), providing an elegant mechanism for the precise control of MICAL activity.

(1) Autoinhibition formation. In the autoinhibited conformation, the CLR region adopts a compact architecture, suppressing MO activity and blocking RBS-I. Notably, steric incompatibility causes partial unfolding of the H3 helix in the RBD (Fig. 1e), disrupting RBS-II. (2) First Rab binding. With the sub- μ M high affinity of Rab binding to RBS-II (Supplementary Fig. 7b), the Rab molecule likely interacts first with RBS-II, reducing the dynamics of H3. This promotes the folding of



the RBD into the compact three-helix structure (Supplementary Fig. 7a), pushing the CH far away from the RBD and resulting in the CLR disassembly. (3) Second Rab binding. Disassociation of the CH domain from the RBD exposes RBS-I, allowing the second Rab molecule to bind. The RBS-I/Rab interaction is sterically incompatible with the tripartite CLR interaction (Fig. 5c), thereby preventing CLR reassembly. Importantly, the second Rab binding alters the N-terminal orientation of the H1 helix, abolishing the binding and inhibitory effect of the RBD on the MO domain (Fig. 5d–f). (4) Full relief of autoinhibition. Dual Rab-binding on the RBD finally leads to complete relief of MICAL autoinhibition, resulting in an extended and open conformation where

the MO is released from the CLR restriction, primed for F-actin binding and modification. The disassembled CH and LIM domains may further facilitate MO activity on actin filaments, given their potential role in F-actin binding^{44,45}.

Such a synergistic Rab binding to MICALs restricts MICAL activation within Rab-enriched compartments, avoiding the devastating effect of hyperactive MICALs on cytoskeleton structure (Fig. 4c). The membrane localization of Rab proteins⁴⁶ further underscores their role in spatially regulating MICAL activity. The requirement of dual Rab-binding in the effective activation of MICALs also explains the reason for the evolutionary duplication of RBS in the RBD of MICALs³⁸.

Fig. 5 | Effective relief of MICAL1 autoinhibition via dual Rab-binding to the RBD. **a–c** Structural comparison of the RBD in the autoinhibited MICAL1 (**a**) with the isolated fragment in apo form (PDB: SLE0) (**b**) or Rab-bound form (PDB: 5LPN) (**c**) by superimposing their H2 helices of the RBDs. Potential atomic clashes between the CH domain in the autoinhibited state and the H3 helix in the apo-RBD or Rab-bound RBD are indicated by dash circles, while the H3 helix in the autoinhibited RBD is missing. Two Rab10 molecules simultaneously bind to the RBD via two Rab-binding sites (RBS-I/II). The binding of Rab10 to RBS-I results in severe atomic clashes with both the CH and LIM domains in autoinhibited MICAL1. **d–f** Structural comparison of the H1 helix in the RBD between the autoinhibited conformation and the Rab-bound form. The rotation of H1 results in a loss of the interaction between the H1 N-terminal part and the MO domain. The key interface residues in the RBD and MO domains are indicated. Notably, the sidechain of F925 in the Rab-bound RBD structure is unassigned. The H2 helix in the RBD was used for

structural alignments in panels (**a–f**). **g, h** NADPH-consumption measurements (**g**) and the statistical analysis (**h**) of MICAL1 and its variants (0.5 μ M) with or without the addition of Rab8a (40 μ M). Rab8a used hereafter is a truncation of Rab8a¹⁻¹⁸¹ with a constitutively active mutation of Q67L, except otherwise indication. The results were normalized against the activity of the MO fragment. The fold-change of enzymatic activity induced by Rab binding for each condition is calculated for comparison. Three independent repeats were performed for each condition. **i** Normalized intensity of pyrene-labeled F-actin disassembled by MICAL1 and its variants (20 nM) with or without the addition of Rab8a (1.6 μ M). Reactions were initiated by adding MICAL protein and NADPH. Mean values from three repeats for each sample were fit with a sigmoidal model to estimate the half-time ($t_{1/2}$) for comparison. Notably, in panels (**g–i**), the construct labeled as 1-1055 indicates the shorter truncation MICAL1¹⁻¹⁰⁵⁵, which deletes the C-terminal 12 residues.

Intriguingly, the autoinhibition and activation mechanisms of MICALS resemble actin-based myosin motors. They all use similar head-to-tail interactions to form autoinhibited conformations and require binding to multiple targets for activation^{47–49}, suggesting a general regulatory strategy in enzyme activation. Notably, in addition to the Rab effectors, F-actin, the substrate of MICALS, has also been indicated to significantly enhance MO activity^{12,37,50,51}. This activation of MICALS by F-actin may involve two mechanisms. Firstly, F-actin acts in concert with specific effectors to relieve MICAL autoinhibition. Secondly, F-actin binding induces a conformational change in the MO domain, promoting its catalytic activity. Thus, future structural study of the MICAL/F-actin complex is required to understand not only how MICALS recognize the F-actin substrate but also how F-actin regulates MICAL activity.

During the transition between autoinhibition and activation of MICALS, the most notable conformational changes occur in the RBD (Fig. 5a–c). Differing from the typical helix bundle, the three helices of the RBD form a relatively flat structure with considerable dynamics (Supplementary Fig. 3e). The remarkable flexibility allows the RBD to switch among different conformations (Fig. 5a–c), accommodating different interactions: binding with the MO domain for autoinhibition, interacting with the CH and LIM domains for the tripartite CLR structure formation, and engaging with various effectors for activation. Thus, the RBD functions as an interaction hub, translating different binding inputs into corresponding MICAL activity outputs.

It is an interesting finding that the assembly of the C-terminal CH, LIM, and RBD domains is required for MICAL1 autoinhibition (Fig. 3c). This highlights the involvement of the CH and LIM domains in suppressing MO activity. Besides the RBD, the CH or LIM domains may contain binding sites for MICALS' regulators, given their roles as interacting modules^{44,45}. Thus, recruiting certain regulators to these domains provides additional mechanisms to disassemble the compact CLR structure for activating MICALS. Interestingly, two MICAL-like proteins (MICAL-L1 and MICAL-L2) have been identified in mammals, which lack the catalytic MO domain yet retain their interactions with Rabs^{10,52,53}. As the tripartite interface residues are also conserved in these MICAL-like proteins (Supplementary Fig. 8c–e), they likely adopt a similar compact CLR structure observed in autoinhibited MICAL1. Thus, the disassembly of the CLR structure via Rab binding may regulate the protein-protein interactions mediated by the CH, LIM, and RBD domains in MICAL-like proteins. This is supported by observations that the CH/RBD and LIM/RBD interactions detected in MICAL-L1 and MICAL-L2 can be disrupted upon Rab13 binding^{54,55}.

Methods

Plasmids

Human MICAL1 and mouse MICAL3 genes were amplified from a cDNA library and then inserted into a pCAG vector with a His₆-Flag tag at the N-terminus for protein purification and a modified pEGFP-C1 vector for cellular assays, respectively. MICAL1 variants with different boundaries

were recombined into a modified pET32a vector with an N-terminal Trx-His₆ tag. Human Rab8a¹⁻¹⁸¹ truncation with a constitutively active mutation of Q67L was codon-optimized, synthesized by Tsingke Biological Technology, and then cloned into a pET28b vector with an N-terminal His₆ tag for protein purification. All the mutants were generated using a QuickChange Site-Directed Mutagenesis Kit, and all plasmids were then sequenced for verification.

Protein expression and purification

The full-length proteins of MICAL1 and their mutants were overexpressed in the mammalian HEK293F expression system. Following a 3-day transfection, cells were harvested and lysed using ultrasonication at an ice bath in a buffer containing 50 mM Tris, pH 7.5, 300 mM NaCl, 5 mM MgCl₂, 0.5% Triton X-100, 2 mM dithiothreitol (DTT), and protease inhibitors (TargetMol, USA). After two rounds of centrifugation at 48,384 \times g for 1 h each, the supernatant was incubated with anti-Flag beads (Smart-Lifesciences) for 2 h. The beads were washed with a wash buffer containing 50 mM Tris, pH 7.5, 300 mM NaCl, 5 mM MgCl₂, and 2 mM DTT. The target protein was then eluted using the wash buffer supplemented with Flag peptide. The elution was concentrated and further purified by size exclusion chromatography (SEC, Superdex 200 Increase 10/300 GL, GE Healthcare) with a buffer containing 50 mM Tris, pH 7.5, 100 mM NaCl, 2 mM MgCl₂, and 2 mM DTT. Following SDS-PAGE analysis, the fractions containing the target proteins were pooled and concentrated for subsequent usage.

The truncations of MICAL1 and Rab8a¹⁻¹⁸¹ were overexpressed in the bacteria expression system. Protein expression was induced by adding 0.2 mM isopropyl- β -D-thiogalactopyranoside (IPTG) at 16 °C overnight in BL21-CodonPlus (DE3) *Escherichia coli* cells. Following induction, the cells were collected and lysed in the lysis buffer (50 mM Tris, pH 7.5, 500 mM NaCl, 5 mM imidazole, and PMSF). After centrifugation, the target proteins in the supernatant were purified using Ni²⁺-nitrilotriacetic acid (NTA) resin (GE Healthcare), followed by treatment with 3C protease to remove the tags. The cleaved proteins were subjected to size exclusion chromatography using a Superdex 200 pg column (GE Healthcare) equilibrated with a buffer containing 50 mM Tris, pH 7.5, 200 mM NaCl, 1 mM DTT, and 1 mM EDTA. The two fragments of MICAL1, MO¹⁻⁴⁸⁹ and MO-CH¹⁻⁶¹⁶, were further purified with an additional cation exchange column (Hitrap SP HP) to remove junk proteins before proceeding to size exclusion chromatography purification.

Negative staining EM

Protein samples (4 μ L) were applied onto a freshly glow-discharged grid. After a 1-minute incubation, the excess protein solution was blotted away using filter paper. Subsequently, 4 μ L of 2% uranyl acetate solution was immediately dropped to the grid for 1-min staining. The grid was then air-dried at room temperature. All the prepared grids were checked and screened by an HT7700 (HITACHI) transmission electron microscope with 100-kV voltage, and the images for 2D-

5-second incubation followed by 3-second blotting with filter paper and then quickly frozen in liquid ethane. These processes were performed using Vitrobot (FEI) at 4 °C with 100% humidity. All prepared grids were stored in liquid nitrogen before sample screening and data collection. Notably, the sample used for initial particle picking was supplemented with 0.15 mM DDM detergent in the buffer condition before freezing.

Grids were carefully transferred to a Titan Krios G3i transmission electron microscope (Thermo Fisher Scientific) at 300 kV, equipped with a Gatan K2 direct electron detector. A total of 18346 movies and 6280 movies of cross-linked MICAL1 protein samples in the general and DDM-containing buffer conditions, respectively, were collected using SerialEM 3.7⁵⁷ in the super-resolution mode with a pixel size of 0.538 Å. Each movie is composed of 32 frames with a 4.6-second exposure. The total dose rate was maintained at 40 electrons/Å² per movie. The defocus range was set from -1.5 to -2.5 μm. In addition, 1018 movies of MICAL1 protein samples without cross-linking were collected for 2D classification during the initial cryo-EM analysis.

Cryo-EM data processing

Cryo-EM data processing in this study was performed using CryoSPARC v3.1⁵⁸. All movies were aligned using MotionCor2⁵⁹ with a B-factor of 150 to produce the micrographs with a physical pixel size of 1.076 Å. After CTF estimation by CTFIND4⁶⁰ with an amplitude contrast of 0.1, 16280 micrographs of cross-linked MICAL1 sample in the general buffer condition were selected by manually removing junks. The particles in the general buffer condition were difficult to pick out accurately, probably due to the small protein size and poor micrograph contrast. The addition of 0.15 mM DDM in the buffer significantly improved particle-picking efficiency, and the sample in this DDM-containing buffer condition was used for initial particle picking and Topaz-training model generation. Consequently, after blob-picking of the particles followed by two rounds of 2D classification, -66736 good particles with a compact shape from -6000 micrographs of cross-linked MICAL1 protein sample in the DDM-containing buffer condition were selected to obtain a deep-learning trained model using Topaz train⁶¹. With this trained model, we initially picked out 9063162 particles from 16280 micrographs of cross-linked MICAL1 protein samples in the general buffer condition, which were further cleaned by several rounds of 2D and 3D classifications, alternatively, and then 78537 good particles in one 3D class with a relatively complete map of the autoinhibited conformation were selected. To further optimize particle orientation, 50 projections were generated from this map as the templates for an additional round of template-based particle picking from the previously processed denoised micrographs. Following similar particle cleaning steps by 2D and 3D classification, two additional good 3D classes containing 67849 and 69871 particles were selected. Then, a combination of three good particle sets from both Topaz and template-based picked particles, along with the removal of duplicate particles with a minimum separation distance of 30 Å and one round of 2D classification, resulted in a total of 122086 best particles.

Due to the relatively small size of MICAL1 protein particles, two parameters, including “Force max over poses/shifts=OFF” and “Batchsize per class = 500”, were implemented in each process of 2D classification. These best particles from the cross-linked MICAL1 protein sample in the general buffer condition were used to generate a high-resolution density map by using non-uniform refinement without additional global/local CTF refinement. Finally, one round of local refinement was performed, tightly focusing on the core regions of the four structured domains to obtain the final density map with an overall resolution of 3.94 Å. The final map was further optimized using DeepEMhancer⁶² with a tightTarget model. The map resolution was estimated using the gold-standard FSC cutoff of 0.143 in cryoSPARC.

Model building and refinement

To obtain an atomic model for autoinhibited MICAL1, we rigidly fit the structures of the fragmented MO (PDB ID: 2BRY), CH (2DK9), LIM (2CO8), and RBD (SLE0) into the final 3.94-Å density map, creating an initial model in UCSF-ChimeraX⁶³. Then, the initial model was manually adjusted in Coot⁶⁴, followed by automatic real-space refinement in Phenix⁶⁵. These procedures were performed iteratively over several rounds to improve the atomic model. The final atomic model was validated against our final cryo-EM density map in Phenix. The statistics for cryo-EM data collection, processing, model refinement, and validation are summarized in Supplementary Table 1. All the figures displaying structural information were prepared using UCSF ChimeraX. To prepare the movie to illustrate the conformational changes of MICAL1 from autoinhibited/closed to open states, a series of step-by-step structural models were manually built to generate the transitions between different states with the command “morph” in UCSF ChimeraX, in which the AlphaFold3⁶⁶-predicted structure of the intact MICAL1-RBD, the crystal structures of MICAL1-MO-CH (4TXI), MICAL1-RBD and Rab10 complex (5LPN) and the cryo-EM structure of autoinhibited MICAL1 in this study were used as references for orientation determination.

NADPH consumption assay

The enzymatic activity of MICAL1 was assessed by monitoring the change in absorbance at 340 nm (A340), corresponding to the conversion of reduced NADPH to oxidized NADP⁺, as MICAL1 uses NADPH as a cofactor for electron transfer in its catalyzed redox reactions⁶⁷. Freshly prepared NADPH was added to the protein buffer to achieve a final concentration of 0.3 mM. After pre-equilibration for 10 min, 10 μL of proteins or protein complexes with indicated concentrations in the figure legends were added to initiate the reaction. The A340 curves were then recorded at 20-second intervals over 1 h using an EnSpire plate reader at 25 °C. Each experiment was repeated three times. The initial slopes of the A340 curves were calculated to compare enzymatic activity across samples.

Pyrene-labeled F-actin disassembly assay

Actin was obtained from rabbit skeletal muscle (Cytoskeleton, USA), according to the manufacturer's instructions. For pyrene labeling, actin was thawed on ice and added with 5 mM DTT in the buffer. Then, it was dialyzed into buffer G (2 mM Tris-HCl, pH 8.0, 0.2 mM CaCl₂, 0.5 mM ATP) overnight at 4 °C. After dialysis, actin was diluted to a concentration of 1.7 mg/mL in buffer G. Actin polymerization was induced by adding a final concentration of 100 mM KCl and 2 mM MgCl₂. Buffer A (100 mM boric acid, pH 8.3, 2 mM MgCl₂, 0.5 mM ATP) was added in an equal volume to the actin solution. N-(1-pyrene) iodoacetamide was dissolved in dimethylformamide at a concentration of 10 mM and then added into the actin solution at a ratio of 7.5 mol N-(1-pyrene) iodoacetamide to 1.0 mol actin. The mixture was rotated at room temperature for 24 h. Labeled actin was collected by centrifugation, and the pellet was homogenized and dialyzed against buffer G supplemented with 0.5 mM DTT for 3 days at 4 °C. The sample was then centrifuged at 4 °C, 10,000 × g centrifuge for 30 min, followed by purification using a size exclusion column (Superdex 200 Increase 10/300GL) equilibrated with buffer G supplemented with 0.5 mM DTT. The concentration of pyrene and actin were determined by measuring absorbances at 344 nm and 290 nm, respectively.

The pyrene-labeled F-actin disassembly assay was carried out as previously described⁶⁸. In brief, pyrene-labeled actin was mixed with unlabeled G-actin to achieve a final concentration of 1 mg/mL, with 10% of the actin labeled. This actin mixture was added with 10× actin polymerization buffer (50 mM Tris-HCl pH 7.5, 500 mM KCl, 20 mM MgCl₂, 10 mM EGTA, 2 mM ATP, and 5 mM DTT) in a 1/40 volume of the mixture and incubated at room temperature for 1 h to promote F-actin formation. Subsequently, the labeled F-actin was diluted to 0.2 mg/mL

using buffer G and aliquoted into a 96-well flat-bottom black polystyrene plate with 150 μL per well. The plate was then transferred to an EnSpire plate reader and shaken for 5 s. Fluorescence signals were recorded at 40-second intervals for 10 min to establish an equilibrium baseline, with an excitation wavelength of 365 nm and an emission wavelength of 407 nm. Following the equilibrium phase, purified MICAL1 samples at a concentration of 20 nM, with or without the addition of 1.6 μM Rab8a and 100 μM NADPH, were added to initiate the reaction. The plate was then monitored for an additional 35 min. To facilitate data normalization, the fluorescence intensity recorded before adding protein and NADPH was designated as 100%, and subsequent readings were normalized accordingly.

F-actin co-sedimentation assay

To assess the binding capacity of different boundaries of MICAL1 to F-actin, a reaction mixture containing 5 μM F-actin and 5 μM various MICAL1 proteins was prepared in a 50 μL reaction volume under the buffer condition (10 mM Tris pH 7.0, 100 mM KCl, 2 mM MgCl_2 , 1 mM DTT, 0.2 mM ATP) and incubated for 1 h at room temperature. The mixture was then centrifuged at $100,000 \times g$ for 20 min at 4 $^\circ\text{C}$ in a TLA-100 ultracentrifuge (Beckman, Krefeld, Germany) to sediment the F-actin and bound MICAL1 proteins. The resulting pellet was resuspended in the same volume of buffer. Finally, equal volumes of the pellet and supernatant samples were loaded onto 12% (w/v) SDS-PAGE gels for electrophoretic separation, and separation results were visualized by staining the gels with Coomassie Brilliant Blue for analysis.

Analytical size exclusion chromatography (aSEC) and static light scattering

The protein samples with a volume of 100 μL were prepared at a final concentration of 100 μM and loaded onto a Superdex 200 Increase 10/300 GL column (GE Healthcare) connected to an ÄKTA pure system (GE Healthcare). The column was equilibrated with the same buffer used in protein purification. To calculate the molecular weight of full-length MICAL1, the elution profile obtained from aSEC was further analyzed using tandem DAWN_HELEOS-II and Optilab T-rEX detectors (Wyatt Technology Corporation, Santa Barbara, CA, USA).

Isothermal titration calorimetry (ITC)

ITC measurements were performed on a PEAQ-ITC Microcal calorimeter (Malvern). The protein samples of Rab8a¹⁻¹⁸¹ and MICAL1^{RBD} or its variants were prepared at a concentration of 200 μM in the syringe and 10 μM in the cell, respectively. All protein samples were prepared in a buffer containing 50 mM Tris pH 7.5, 100 mM NaCl, 2 mM MgCl_2 , and 1 mM DTT. During the titration, 2 μL of the protein sample in the syringe was injected into the cell each time. An interval of 150 s between two injections was set to ensure the curve returned to the baseline. The titration data were analyzed and fitted using a two-site binding model to determine the binding parameters.

Cell culture and transfection

HeLa cells were cultured in Dulbecco's Modified Eagle's Medium (DMEM) supplemented with 10% Fetal Bovine Serum (FBS), 1% Penicillin-Streptomycin Solution, and 1% Non-Essential Amino Acids (NEAA). The cells were maintained at 37 $^\circ\text{C}$ in an incubator with 5% CO_2 . Lipofectamine 3000 reagent (Thermo Fisher Scientific) was used for transfection.

HEK293F cells were cultured in 293 Chemically Defined Medium (Union) and maintained at 37 $^\circ\text{C}$ in an incubator with 5% CO_2 . Polyethylenimine Linear (PEI) MW40000 (YEASEN) was used for transfection.

Immunofluorescence and imaging

HeLa cells transfected with the indicated plasmids for 24 h were seeded onto glass coverslips pre-treated with 10 mg/mL fibronectin for

1 h. After a 12-hour additional culture, the cells were fixed with 4% paraformaldehyde (PFA) for 15 min at 37 $^\circ\text{C}$, treated with 0.1% Triton X-100 for 10 min at room temperature, and blocked in 2% Bovine Serum Albumin (BSA) for 30 min. Cellular F-actin was stained by Alexa Fluor TM 594 phalloidin (Thermo Fisher Scientific). The cells were visualized and recorded with 100 \times objective using a Nikon A1R Confocal Microscope. NIS-Elements A1R Analysis software was used to calculate the intensity of phalloidin-stained cellular actin filaments and cell size. The overexpression protein levels of wild-type and mutated MICAL1 in HeLa cells were comparable, confirmed by western blotting.

Statistics and reproducibility

All values are displayed as the mean values with an error bar of standard deviation (SD). Significance was calculated using an unpaired, two-tailed, student *t* tests model. $P > 0.05$ was considered as not significant (ns), while $P < 0.05$ was indicated as *, $P < 0.01$ as **, $P < 0.001$ as ***, $P < 0.0001$ as ****. All statistical calculations were performed and exported to figures using Graph Prim 8.3 and Origin 2019. The protein analysis results are representative of at least three independent repeats, and 20–30 cells for each condition were used for cellular analysis.

Reporting summary

Further information on research design is available in the Nature Portfolio Reporting Summary linked to this article.

Data availability

The cryo-EM density map of MICAL1 has been deposited into EMDB with accession code [EMD-38989](#), and the corresponding atomic model has also been deposited in PDB with accession code [8Y6K](#). Source data for the figures and Supplementary Figs. are provided as a Source Data file. Source data are provided with this paper.

References

- Schaks, M., Giannone, G. & Rottner, K. Actin dynamics in cell migration. *Essays Biochem* **63**, 483–495 (2019).
- Rizzelli, F., Malabarba, M. G., Sigismund, S. & Mapelli, M. The crosstalk between microtubules, actin and membranes shapes cell division. *Open Biol.* **10**, 190314 (2020).
- Smythe, E. & Ayscough, K. R. Actin regulation in endocytosis. *J. Cell Sci.* **119**, 4589–4598 (2006).
- Titus, M. A. Myosin-driven intracellular transport. *Cold Spring Harb. Perspect. Biol.* **10**, a021972 (2018).
- Pollard, T. D. Actin and actin-binding proteins. *Cold Spring Harb. Perspect. Biol.* **8**, a018226 (2016).
- Welch, M. D., DePace, A. H., Verma, S., Iwamatsu, A. & Mitchison, T. J. The human Arp2/3 complex is composed of evolutionarily conserved subunits and is localized to cellular regions of dynamic actin filament assembly. *J. Cell Biol.* **138**, 375–384 (1997).
- Andrianantoandro, E. & Pollard, T. D. Mechanism of actin filament turnover by severing and nucleation at different concentrations of ADF/cofilin. *Mol. Cell* **24**, 13–23 (2006).
- dos Remedios, C. G. et al. Actin binding proteins: regulation of cytoskeletal microfilaments. *Physiol. Rev.* **83**, 433–473 (2003).
- Suzuki, T. et al. MICAL, a novel CasL interacting molecule, associates with vimentin. *J. Biol. Chem.* **277**, 14933–14941 (2002).
- Terman, J. R., Mao, T., Pasterkamp, R. J., Yu, H. H. & Kolodkin, A. L. MICALs, a family of conserved flavoprotein oxidoreductases, function in plexin-mediated axonal repulsion. *Cell* **109**, 887–900 (2002).
- Hung, R. J. et al. Mical links semaphorins to F-actin disassembly. *Nature* **463**, 823–827 (2010).
- Hung, R. J., Pak, C. W. & Terman, J. R. Direct redox regulation of F-actin assembly and disassembly by Mical. *Science* **334**, 1710–1713 (2011).

13. Rich, S. K., Baskar, R. & Terman, J. R. Propagation of F-actin disassembly via Myosin15-Mical interactions. *Sci. Adv.* **7**, eabg0147 (2021).
14. Van Battum, E. Y. et al. The intracellular redox protein MICAL-1 regulates the development of hippocampal mossy fibre connections. *Nat. Commun.* **5**, 4317 (2014).
15. Schmidt, E. F., Shim, S. O. & Strittmatter, S. M. Release of MICAL autoinhibition by semaphorin-plexin signaling promotes interaction with collapsin response mediator protein. *J. Neurosci.* **28**, 2287–2297 (2008).
16. Grigoriev, I. et al. Rab6, Rab8, and MICAL3 cooperate in controlling docking and fusion of exocytotic carriers. *Curr. Biol.* **21**, 967–974 (2011).
17. Liu, Q. et al. MICAL3 flavoprotein monooxygenase forms a complex with centralspindlin and regulates cytokinesis. *J. Biol. Chem.* **291**, 20617–20629 (2016).
18. Frémont, S. et al. Oxidation of F-actin controls the terminal steps of cytokinesis. *Nat. Commun.* **8**, 14528 (2017).
19. Niu, F., Sun, K., Wei, W., Yu, C. & Wei, Z. F-actin disassembly factor MICAL1 binding to Myosin Va mediates cargo unloading during cytokinesis. *Sci. Adv.* **6**, eabb1307 (2020).
20. Ashida, S. et al. Expression of novel molecules, MICAL2-PV (MICAL2 prostate cancer variants), increases with high Gleason score and prostate cancer progression. *Clin. Cancer Res.* **12**, 2767–2773 (2006).
21. Barravecchia, I. et al. Enriching the arsenal of pharmacological tools against MICAL2. *Molecules* **26**, 7519 (2021).
22. Alto, L. T. & Terman, J. R. MICALs. *Curr. Biol.* **28**, R538–R541 (2018).
23. Rajan, S. et al. Disassembly of bundled F-actin and cellular remodeling via an interplay of Mical, cofilin, and F-actin crosslinkers. *Proc. Natl. Acad. Sci. USA* **120**, e2309955120 (2023).
24. Hung, R. J., Spaeth, C. S., Yesilyurt, H. G. & Terman, J. R. SelR reverses Mical-mediated oxidation of actin to regulate F-actin dynamics. *Nat. Cell Biol.* **15**, 1445–1454 (2013).
25. Lee, B. C. et al. MsrB1 and MICALs regulate actin assembly and macrophage function via reversible stereoselective methionine oxidation. *Mol. Cell* **51**, 397–404 (2013).
26. Sjöblom, T. et al. The consensus coding sequences of human breast and colorectal cancers. *Science* **314**, 268–274 (2006).
27. Dazzo, E. et al. Mutations in MICAL-1 cause autosomal-dominant lateral temporal epilepsy. *Ann. Neurol.* **83**, 483–493 (2018).
28. Prifti, E. et al. Mical modulates Tau toxicity via cysteine oxidation in vivo. *Acta Neuropathol. Commun.* **10**, 44 (2022).
29. Yoon, J. & Terman, J. R. MICAL redox enzymes and actin remodeling: new links to classical tumorigenic and cancer pathways. *Mol. Cell Oncol.* **5**, e1384881 (2018).
30. Vanoni, M. A., Vitali, T. & Zucchini, D. MICAL, the flavoenzyme participating in cytoskeleton dynamics. *Int. J. Mol. Sci.* **14**, 6920–6959 (2013).
31. Vanoni, M. A. Structure-function studies of MICAL, the unusual multidomain flavoenzyme involved in actin cytoskeleton dynamics. *Arch. Biochem. Biophys.* **632**, 118–141 (2017).
32. Rajan, S., Terman, J. R. & Reisler, E. MICAL-mediated oxidation of actin and its effects on cytoskeletal and cellular dynamics. *Front Cell Dev. Biol.* **11**, 1124202 (2023).
33. Giridharan, S. S., Rohn, J. L., Naslavsky, N. & Caplan, S. Differential regulation of actin microfilaments by human MICAL proteins. *J. Cell Sci.* **125**, 614–624 (2012).
34. Esposito, A. et al. Human MICAL1: Activation by the small GTPase Rab8 and small-angle X-ray scattering studies on the oligomerization state of MICAL1 and its complex with Rab8. *Protein Sci.* **28**, 150–166 (2019).
35. Nadella, M., Bianchet, M. A., Gabelli, S. B., Barrila, J. & Amzel, L. M. Structure and activity of the axon guidance protein MICAL. *Proc. Natl. Acad. Sci. USA* **102**, 16830–16835 (2005).
36. Siebold, C. et al. High-resolution structure of the catalytic region of MICAL (molecule interacting with CasL), a multidomain flavoenzyme-signaling molecule. *Proc. Natl. Acad. Sci. USA* **102**, 16836–16841 (2005).
37. Alqassim, S. S. et al. Modulation of MICAL Monooxygenase Activity by its Calponin Homology Domain: Structural and Mechanistic Insights. *Sci. Rep.* **6**, 22176 (2016).
38. Rai, A. et al. bMERB domains are bivalent Rab8 family effectors evolved by gene duplication. *Elife* **5**, e18675 (2016).
39. Kim, J. et al. Structural and kinetic insights into flavin-containing monooxygenase and calponin-homology domains in human MICAL3. *IUCr* **7**, 90–99 (2020).
40. Jia, X. et al. Crystal structure of the SH3 domain of ASAP1 in complex with the proline rich motif (PRM) of MICAL1 reveals a unique SH3/PRM interaction mode. *Int. J. Mol. Sci.* **24**, 1414 (2023).
41. Sun, H. et al. Solution structure of calponin homology domain of Human MICAL-1. *J. Biomol. NMR* **36**, 295–300 (2006).
42. Choi, Y., Agarwal, S. & Deane, C. M. How long is a piece of loop? *PeerJ* **1**, e1 (2013).
43. Haikazian, S. & Olson, M. F. MICAL1 monooxygenase in autosomal dominant lateral temporal epilepsy: role in cytoskeletal regulation and relation to cancer. *Genes (Basel)* **13**, 715 (2022).
44. Yin, L. M., Schnoor, M. & Jun, C. D. Structural characteristics, binding partners and related diseases of the calponin homology (CH) domain. *Front Cell Dev. Biol.* **8**, 342 (2020).
45. Anderson, C. A., Kovar, D. R., Gardel, M. L. & Winkelman, J. D. LIM domain proteins in cell mechanobiology. *Cytoskeleton (Hoboken)* **78**, 303–311 (2021).
46. Stenmark, H. Rab GTPases as coordinators of vesicle traffic. *Nat. Rev. Mol. Cell Biol.* **10**, 513–525 (2009).
47. Niu, F. et al. Autoinhibition and activation mechanisms revealed by the triangular-shaped structure of myosin Va. *Sci. Adv.* **8**, eadd4187 (2022).
48. Scarff, C. A. et al. Structure of the shutdown state of myosin-2. *Nature* **588**, 515–520 (2020).
49. Yang, S. et al. Cryo-EM structure of the inhibited (10S) form of myosin II. *Nature* **588**, 521–525 (2020).
50. Zucchini, D., Caprini, G., Pasterkamp, R. J., Tedeschi, G. & Vanoni, M. A. Kinetic and spectroscopic characterization of the putative monooxygenase domain of human MICAL-1. *Arch. Biochem. Biophys.* **515**, 1–13 (2011).
51. Wu, H., Yesilyurt, H. G., Yoon, J. & Terman, J. R. The MICALs are a Family of F-actin Dismantling Oxidoreductases Conserved from *Drosophila* to Humans. *Sci. Rep.* **8**, 937 (2018).
52. Yamamura, R., Nishimura, N., Nakatsuji, H., Arase, S. & Sasaki, T. The interaction of JRAB/MICAL-L2 with Rab8 and Rab13 coordinates the assembly of tight junctions and adherens junctions. *Mol. Biol. Cell* **19**, 971–983 (2008).
53. Sharma, M., Giridharan, S. S., Rahajeng, J., Naslavsky, N. & Caplan, S. MICAL-L1 links EHD1 to tubular recycling endosomes and regulates receptor recycling. *Mol. Biol. Cell* **20**, 5181–5194 (2009).
54. Abou-Zeid, N. et al. MICAL-like1 mediates epidermal growth factor receptor endocytosis. *Mol. Biol. Cell* **22**, 3431–3441 (2011).
55. Miyake, K. et al. Actin cytoskeletal reorganization function of JRAB/MICAL-L2 is fine-tuned by intramolecular interaction between first LIM zinc finger and c-terminal coiled-coil domains. *Sci. Rep.* **9**, 12794 (2019).
56. Chu, X. et al. Annealing synchronizes the 70S ribosome into a minimum-energy conformation. *Proc. Natl. Acad. Sci. USA* **119**, e2111231119 (2022).
57. Mastronarde, D. N. Automated electron microscope tomography using robust prediction of specimen movements. *J. Struct. Biol.* **152**, 36–51 (2005).

58. Punjani, A., Rubinstein, J. L., Fleet, D. J. & Brubaker, M. A. cryoSPARC: algorithms for rapid unsupervised cryo-EM structure determination. *Nat. Methods* **14**, 290–296 (2017).
59. Zheng, S. Q. et al. MotionCor2: anisotropic correction of beam-induced motion for improved cryo-electron microscopy. *Nat. Methods* **14**, 331–332 (2017).
60. Rohou, A. & Grigorieff, N. CTFFIND4: fast and accurate defocus estimation from electron micrographs. *J. Struct. Biol.* **192**, 216–221 (2015).
61. Bepler, T., Kelley, K., Noble, A. J. & Berger, B. Topaz-Denoise: general deep denoising models for cryoEM and cryoET. *Nat. Commun.* **11**, 5208 (2020).
62. Sanchez-Garcia, R. et al. DeepEMhancer: a deep learning solution for cryo-EM volume post-processing. *Commun. Biol.* **4**, 874 (2021).
63. Pettersen, E. F. et al. UCSF ChimeraX: structure visualization for researchers, educators, and developers. *Protein Sci.* **30**, 70–82 (2021).
64. Emsley, P., Lohkamp, B., Scott, W. G. & Cowtan, K. Features and development of Coot. *Acta Crystallogr. D Biol. Crystallogr.* **66**, 486–501 (2010).
65. Liebschner, D. et al. Macromolecular structure determination using X-rays, neutrons and electrons: recent developments in Phenix. *Acta Crystallogr. D Struct. Biol.* **75**, 861–877 (2019).
66. Abramson, J. et al. Accurate structure prediction of biomolecular interactions with AlphaFold3. *Nature* **630**, 493–500 (2024).
67. Vitali, T., Maffioli, E., Tedeschi, G. & Vanoni, M. A. Properties and catalytic activities of MICAL1, the flavoenzyme involved in cytoskeleton dynamics, and modulation by its CH, LIM and C-terminal domains. *Arch. Biochem Biophys.* **593**, 24–37 (2016).
68. Yoon, J., Hung, R. J. & Terman, J. R. Characterizing F-actin disassembly induced by the semaphorin-signaling component MICAL. *Methods Mol. Biol.* **1493**, 119–128 (2017).

Acknowledgements

We thank the assistance of Southern University of Science and Technology (SUSTech) Cryo-EM Center and Core Research Facilities. This work was supported by the Key-Area Research and Development Program of Guangdong Province (Grant No. 2023B0303010001 to Z.W.), the National Natural Science Foundation of China (Grant No. 31971131 to Z.W. and 32170697 and 32370743 to C.Y.), Guangdong Basic and Applied Basic Research Foundation (Grant No. 2023A1515030232 and 2024A1515012651 to F.N.), Shenzhen Science and Technology Program (Grant No. RCJC20210609104333007 to Z.W. and 20231121095506001 to C.Y.), Shenzhen Key Laboratory of Biomolecular Assembling and Regulation (Grant No. ZDSYS2022040211100001 to Z.W.). Z.W. and C.Y. are investigators of SUSTech Institute for Biological Electron Microscopy.

Author contributions

Z.W. and F.N. conceived the study. Z.W. supervised the project. L.L., J.D., S.X., J.X. and F.N. designed and performed experiments. L.L., J.D., C.Y., F.N. and Z.W. analyzed the data. F.N. and Z.W. wrote the manuscript with inputs from other authors.

Competing interests

The authors declare no competing interests.

Additional information

Supplementary information The online version contains supplementary material available at <https://doi.org/10.1038/s41467-024-50940-7>.

Correspondence and requests for materials should be addressed to Fengfeng Niu or Zhiyi Wei.

Peer review information *Nature Communications* thanks the anonymous reviewers for their contribution to the peer review of this work. A peer review file is available.

Reprints and permissions information is available at <http://www.nature.com/reprints>

Publisher's note Springer Nature remains neutral with regard to jurisdictional claims in published maps and institutional affiliations.

Open Access This article is licensed under a Creative Commons Attribution-NonCommercial-NoDerivatives 4.0 International License, which permits any non-commercial use, sharing, distribution and reproduction in any medium or format, as long as you give appropriate credit to the original author(s) and the source, provide a link to the Creative Commons licence, and indicate if you modified the licensed material. You do not have permission under this licence to share adapted material derived from this article or parts of it. The images or other third party material in this article are included in the article's Creative Commons licence, unless indicated otherwise in a credit line to the material. If material is not included in the article's Creative Commons licence and your intended use is not permitted by statutory regulation or exceeds the permitted use, you will need to obtain permission directly from the copyright holder. To view a copy of this licence, visit <http://creativecommons.org/licenses/by-nc-nd/4.0/>.

© The Author(s) 2024